ACS Catalysis

Research Article

pubs.acs.org/acscatalysis

Exploiting the Photonic Crystal Properties of TiO_2 Nanotube Arrays To Enhance Photocatalytic Hydrogen Production

Gian Luca Chiarello,*[,†] Alessio Zuliani,[†] Davide Ceresoli,[‡] Rocco Martinazzo,[†] and Elena Selli[†]

[†]Università degli Studi di Milano, Dipartimento di Chimica, via Golgi 19, I-20133 Milano, Italy

[‡]CNR-ISTM, Institute of Molecular Sciences and Technologies, via Golgi 19, I-20133 Milano, Italy

Supporting Information

ABSTRACT: Two series of self-assembled TiO_2 nanotube (NT) arrays were grown by electrochemical anodization on a metallic titanium substrate with different anodization times and applied potentials in HF-containing ethylene glycol electrolyte solutions and postcalcined at 450 °C. The obtained thin films were characterized by FESEM, XRD, and UV−vis−NIR DRS analyses and tested as photoanodes in incident photon to current efficiency (IPCE) measurements and in a two-compartment photoelectrochemical cell (PEC) for separate H_2 and O_2 production. The photocatalytic performance of the NT arrays significantly increased with an increase in the potential applied during anodization (i.e., with increasing the NT inner diameter) and the incident angle of the light. IPCE measurements revealed that such unexpected behavior is due to a red shift of the activity threshold that allows harvesting and converting a larger portion of the solar spectrum. This phenomenon is ascribed to the parallel shift of the photonic band gap position originated by the intrinsic photonic crystal properties and demonstrates the important role played by ordered hierarchical structures in improving the photocatalytic performance of NT arrays by confining and manipulating light.

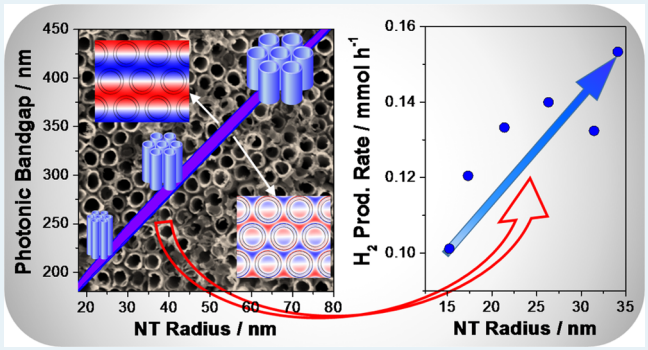

KEYWORDS: *photocatalytic water splitting, photoelectrochemical cell, TiO_2 nanotubes, photonic crystals, photonic bandgap, electrochemical anodization*

1. INTRODUCTION

Photoelectrochemical cells (PECs) are the most promising devices for solar energy harvesting and storage in the form of hydrogen as a solar fuel, because they allow water cleavage with separate H_2 and O_2 production.[1−6] Fabrication of stable and efficient photoelectrodes is the crucial task for the future development and application of such devices. Thin films consisting of self-assembled, vertically oriented TiO_2 nanotube (NT) arrays, directly grown on a conductive Ti foil by electrochemical anodization,[7,8] represent an attractive and cost-effective method to prepare photoanodes.[6,9−12] Their well-organized architecture provides (i) efficient percolation pathways for vectorial transfer of photopromoted electrons, ensuring effective charge separation, (ii) large internal surface area which guarantees enhanced photon absorption and reactant adsorption on the photoactive surface, and (iii) optimal adhesion of the photoactive film to the conductive support, ensuring high stability and improved electron transfer.

The ordered 2D structure of the NT arrays confers them the photonic crystal properties due to the periodic modulation of the dielectric constant.[13−15] This determines the formation of a photonic band gap (PBG), i.e. a range of forbidden frequencies in certain directions that are totally reflected and cannot propagate through the periodic structure, due to Bragg diffraction and scattering. Moreover, the electromagnetic field is predominantly localized in the low-dielectric material (air or water) at the blue edge of the PBG (air band), whereas it is predominantly localized on the high-dielectric material (TiO_2 NT walls) at the red edge (dielectric band). Third, a photonic crystal structure induces the flattening of the air and dielectric bands in some directions. Because the group velocity of the photons is proportional to the slope of the dispersion curves, light travels at a vanishing speed when the photonic bands are flat, generating the so-called "slow photons".[14,15]

Hence, the PBG can in principle be exploited in photocatalysis to confine, control, and manipulate photons with the intent to intensify the efficiency of light harvesting and absorption. The major effort in this field has been addressed toward 3D TiO_2 inverse opal structures.[16−21] However, only in a few reports[22,23] have the photonic crystal properties of TiO_2 NT films been explored for photocatalytic applications, despite the large number of publications on this topic. This is rather surprising, also because the physicochemical properties and morphology of NTs can be easily tailored by controlling the synthesis parameters such as the anodization time, the applied

Received: December 11, 2015
Revised: January 13, 2016
Published: January 15, 2016

DOI: 10.1021/acscatal.5b02817
ACS Catal. 2016, 6, 1345−1353

DC voltage, the electrolyte composition, and the thermal post-treatment conditions.[7]

In this work we show, with the support of theoretical calculations, that the PBG position and width are affected by the NT inner diameter, wall thickness, and the distance between the tubes. Thus, the PBG can be easily tuned in order to maximize the light-harvesting efficiency, especially at the absorption edge. In particular, a linear red shift of the photoactivity edge with a consequently up to 50% increased photocatalytic H_2 production rate under polychromatic irradiation was attained by simply increasing the NT inner diameter (i.e., red shifting the PBG) without any chemical doping or electronic structure modification.

2. METHODS

2.1. Preparation of TiO_2 NT Films. Thin films of vertically oriented TiO_2 nanotube (NT) arrays self-assembled on a conductive Ti support were prepared by electrochemical anodization. A homemade electrochemical cell was employed consisting of a PVC conical bath with a 40 mm diameter hole at the bottom, placed on a stainless steel support. The hole is closed underneath with a 45 × 45 mm^2 Ti foil (Advent, temper annealed, purity 99.6%, thickness 100 μm), firmly sealed against an O ring by a screw with a Plexiglas plaque on top. A copper wire is inserted between the Ti foil and the Plexiglas to ensure electrical contact. A 45 × 45 mm^2 Pt mesh (Goodfellow, 0.25 mm aperture, 65% open area) was used as a counter electrode to allow the release of hydrogen gas produced underneath during the anodization process. The Pt mesh was immersed in the electrolyte solution and suspended 20 mm above the Ti foil. The Ti foil (anode) and the Pt counter electrode (cathode) were connected to a EA-PS 2384-05B power supply and a Tektronix DMM4040 digital multimeter. Prior to anodization, the Ti foils were degreased and cleaned with acetone, then with methanol, and finally with Milli-Q water in an ultrasonic bath for 15 min each.

A two-anodization process was employed in order to obtain more homogeneous TiO_2 NT films. During the first step, the samples were anodized at 35 V for 120 min in a 1.0 M H_2O + 0.1 M NH_4F in ethylene glycol electrolyte solution. The obtained TiO_2 NT film was removed by ultrasonic treatment in water. This step flattens the Ti foil surface and leaves a pattern of little grooves that helps the formation of more homogeneous NT films during the second anodization. A 8.0 M H_2O + 0.2 M HF in ethylene glycol electrolyte solution was used during the second anodization. In order to study the effect of the anodization time and applied voltage, two series of samples were prepared. In the first series the anodization time was changed from 10 to 240 min, with a fixed applied voltage of 50 V. Because the NT growing rate increases with an increase in the applied voltage, in the second series the voltage was changed from 30 V up to 80 V while the anodization time was decreased, in order to obtain ca. 1 μm long TiO_2 NTs. After the second anodization, the samples were washed in ethanol in the ultrasonic bath for 15 min and calcined in an oven at 450 °C for 2 h, with a heating ramp of 10 °C min^{-1}.

2.2. Characterization of TiO_2 NT Films. Scanning electron microscopy (SEM) analysis was carried out on a LEICA LEO 1430 instrument. Field emission scanning electron microscopy (FESEM) images were obtained with a ZEISS Supra40 apparatus. X-ray diffraction patterns were recorded on a Philips PW3020 powder diffractometer, by using Cu Kα radiation (λ = 1.5418 Å). UV−vis−NIR diffuse reflectance (DR) spectra were recorded in the 220 nm < λ < 2600 nm range with a Shimadzu UV3600 Plus spectrophotometer equipped with an ISR-603 integrating sphere.

2.3. IPCE Measurements. Incident photon to current efficiency (IPCE) was measured on an optical bench equipped with a 300 W Xe lamp (Lot-Oriel), a monochromator (LOT-Oriel Omni-λ 150), a shutter (Thorlabs SC10), and a homemade Plexiglas cell with an optical Pyrex glass window. A 25 × 25 mm^2 platinum foil (cathode) was used as the counter electrode and placed below the irradiated TiO_2 NT film (anode). Both the cathode and anode were immersed in a 1.0 M NaOH electrolyte solution and connected through an external circuit to a digital multimeter (Tektronix DMM4040). The photocurrent was measured without any external applied voltage (i.e. at zero bias) in the 250−550 nm wavelength range with a 2 nm step and a 4 s time per step. The incident light power was measured with the same scan parameters using a calibrated Thorlabs S130VC photodiode connected to a Thorlabs PM200 power meter placed at exactly the same distance as the TiO_2 NT film, with the Pyrex window in between to account for the transmittance of the cell window. The percent IPCE at each wavelength was calculated employing the formula

$$\%\,\mathrm{IPCE} = \frac{I_\lambda}{P_\lambda} \times \frac{1240}{\lambda} \times 100$$

where I_λ is the photocurrent density (mA cm^{-2}) measured with the digital multimeter at a specific incident wavelength λ (nm) and divided by the illuminated area of the film, P_λ is the incident power density (mW cm^{-2}) measured with the photodiode at the same λ, and 1240 (J nm C^{-1}) = hce^{-1}, h being the Planck constant, c the speed of light, and e the charge of a single electron.

2.4. Angularly Resolved Measurements. The setup used for studying the effect of the incident light angle is schematically shown in Figure S1 in the Supporting Information. In particular, the NT film was connected to an alligator clip and mounted on a rotating holder with a goniometer on top. The Pt counter electrode was placed at 90° with respect to the NT film. Both electrodes were connected to the digital multimeter and immersed in a cylindrical Pyrex vessel containing a 1.0 M NaOH electrolyte solution. The monochromator slit was adjusted at 1.7 mm in order to minimize the band full width at half-maximum, as measured with a compact spectrometer (Thorlabs CCS100). The beam exits the monochromator with 4° divergence; thus, it was collimated with an UV Fused Silica Bi-Convex lens (Thorlabs LB4879-A). The collimation lens is also necessary to significantly decrease the illuminated area variation on the sample with increasing incident angle thanks to the shrinking of the spot size (Figure S2 in the Supporting Information). In contrast, this lens cuts the light with λ <300 nm. The photocurrent was measured without any external applied voltage in the 280−450 nm wavelength range with a 2 nm step and a 4 s time per step.

2.5. Separate H_2 and O_2 Photocatalytic Production Tests. The synthesized TiO_2 NT films were tested as photoanodes in a two-compartment photocatalytic cell for separate H_2 and O_2 production similar to that already described.[5] The cell allows one to simultaneously measure the evolved gases and the photocurrent at zero bias. In particular, the TiO_2 NT photoanode was immersed in a 0.5 M

DOI: 10.1021/acscatal.5b02817
ACS Catal. 2016, 6, 1345−1353

H_2SO_4 solution (anodic compartment) and connected to a Pt counter electrode immersed in a 1.0 M NaOH solution (cathodic compartment), by an external circuit including a digital Tektronix DMM4040 multimeter. The two compartments were separated by an ion exchange Nafion 117 membrane. The irradiation source was an iron halogenide mercury arc lamp (Jelosil HG200, 250 W) emitting in the 350 nm < λ < 450 nm range, with a full irradiation intensity of ca. 32 mW cm^{-2}. The emission spectrum of the lamp was measured by means of a Thorlabs CCS100 spectrometer with a compact CCD. The evolved H_2 and O_2 were collected in two graduated burets surmounting the two electrodes, initially filled with the two electrolyte solutions; their volume was measured every 30 min of irradiation from the volume displacement of the liquid inside the burets. No electrical bias or sacrificial agent was ever employed during the tests.

2.6. Computational Methods. The photonic band structure and the electromagnetic modes were calculated employing the MIT Photonic-Bands code (MPB).[24] The TiO_2 NTs periodic structures were modeled as a continuum with a frequency-independent isotropic dielectric constant of 7.1 or 11.7, corresponding to those of anatase at 3 eV (i.e., just below the absorption edge) or 4 eV (i.e., above the absorption edge where the imaginary part is still negligible), respectively, as reported by Jellison et al.[25] The adopted simulation setup was purely two-dimensional (i.e., assuming NTs of infinite length and light traveling *parallel* to the film) with a periodic array of spatially separated hollow cylinders with a hexagonal lattice arrangement. The effect of the geometrical parameters on the photonic band gap position was investigated by varying the inner radius in the range 10−100 nm, the wall thickness between 6 and 20 nm and the gap between the tubes from 10 to 40 nm. When varying one parameter the other two were set as follows: the inner radius at 50 nm, the tube thickness at 10 nm, and the distance between tube walls at 20 nm. The empty space was assumed to have a dielectric constant of 1.7, to model the effect of interstitial water. A full model accounting for the shape of the NTs, their finite length, and the frequency dependence of the dielectric permittivity is not possible at present and would in any event miss the primary role of the light scattered by impurities and imperfections.

3. RESULTS AND DISCUSSION

3.1. Morphology of TiO_2 NT Arrays. TiO_2 NTs growth during Ti anodization in organic solvents containing water and fluoride ions proceeds through two steps: i.e., (i) the electric-field-assisted formation of a dense TiO_2 layer at the metal surface, according to the reaction $Ti + 2H_2O \rightarrow TiO_2 + 2H^+ + 2e^-$ and (ii) the dissolution at the oxide/electrolyte interface of the so produced oxide layer, due to the formation of the soluble $Ti[F_6]^{2-}$ complex.[7] The dissolution is both field-assisted and chemical, but while the former takes place at the NTs bottom, the latter can occur along the whole NT surface. At the same time, H_2 evolution occurs at the Pt cathode. Because of the competition between oxide formation and its dissolution, NT formation can be obtained only in the presence of an optimal fluoride concentration (usually 0.05 M < $[F^-]$ < 0.5 M). Different morphology aspects of typical TiO_2 NTs can be appreciated in Figure 1, showing several SEM images obtained from a NT film etched by gently scratching it with a cutter tip (Figure 1A).

By this way small fragments of the film were detached, which randomly rotated over the NT film surface, as shown in Figure 1C,F. In particular, Figure 1C displays a SEM micrograph of a film fragment rotated by 180° showing the typical closed and hemispherically shaped bottom of the NTs, together with a limited view of the NT cross section (lower part of Figure 1C), revealing the characteristic inner V shape of TiO_2 NTs (i.e., their wall thickness increases toward the bottom).[26,27] Moreover, the thickness of the NT bottom (the barrier layer) increases with increasing anodization time and applied potential.[28]

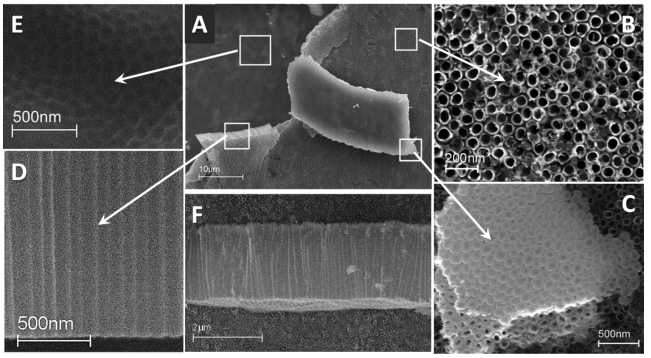

Figure 1. (A) SEM image along a mechanical scratch over a TiO_2 NT film with the magnification of (B) the top, (C) the bottom, and (D) the side views of the NTs, together with (F) a fragment of NT film showing the film thickness and of (E) the metal Ti surface underneath the NT film.

The detachment of the NT film leaves a pattern of little grooves on the metal Ti surface (Figure 1E) specular to the NTs bottom. In the two-step anodization process adopted in the present work, the formation of this pattern is exploited to obtain a more homogeneous and better-aligned NT array. The top view of the NT film (Figure 1B) shows a rather homogeneous surface characterized by the hexagonally shaped, closely packed NT open mouths. The fragments rotated by 90° (Figure 1 F,D) exhibit the side morphology of the NT array consisting of well self-assembled and vertically aligned individual NTs. These micrographs were used to measure the thickness of the TiO_2 NT films (i.e., the NT length).

Figure 2 shows that, as expected, the NT length linearly increases with an increase in the anodization time under the anodization conditions adopted here, up to ca. 120 min. After 2 h the NT growth rate decreases with increasing anodization time because chemical dissolution becomes predominant, leading to an extended etching of the NT top. Moreover, a

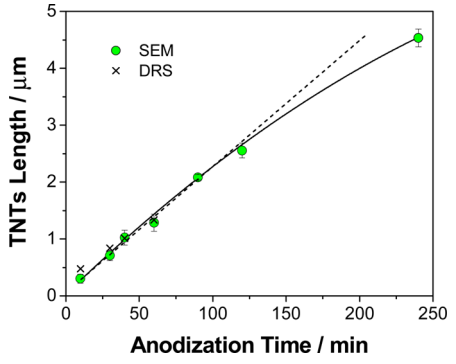

Figure 2. Length of TiO_2 NTs determined from SEM micrographs and by UV−vis−NIR DR spectroscopy as a function of the anodization time under 50 V constant applied potential.

DOI: 10.1021/acscatal.5b02817
ACS Catal. 2016, 6, 1345−1353

prolonged exposure to the fluoride-containing electrolyte leads to the appearance of undesired irregularly shaped oxide aggregates laying over the top of the tubes, commonly called "nanograss".[6,7] The NT growth rate, which can be obtained from the slope of the linear part of the curve shown in Figure 2, is also affected, among other parameters, by the potential applied during the anodization process. Furthermore, by an increase in the anodization potential both the inner NT diameter (Figures 3 and 4) and the NT growth rate (Figure 3) linearly increase.

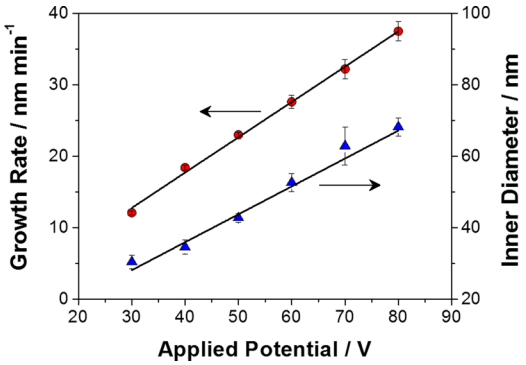

Figure 3. Effect of the applied potential on the NTs growth rate and inner diameter during the Ti anodization.

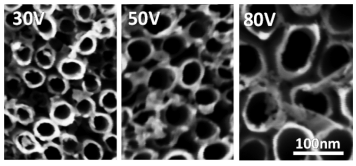

Figure 4. Top view FESEM micrographs of TiO_2 NT arrays synthesized by Ti anodization in a H_2O- and HF-containing ethylene glycol electrolyte solution at 30, 50, and 80 V for 1.21, 0.72, and 0.45 h, respectively.

Moreover, Figure 4 shows that the wall thickness (ca. 10 ± 1 nm) at the top of the TiO_2 NTs is not substantially affected by the applied potential, at least under the experimental conditions investigated here and applied potential range.

3.2. XRD Investigation. The as-prepared self-assembled, vertically oriented TiO_2 NT arrays are notoriously amorphous, their XRD patterns being dominated by the reflections of the metal Ti foil underneath. A postcalcination treatment is therefore necessary to confer them the crystallinity required for photocatalytic applications. The main peaks of crystalline TiO_2 appear after calcination at 450 °C (Figure 5). Their intensity increases with an increase in the anodization time, whereas those of the Ti foil decrease in parallel, in agreement with the increasing thickness of the NT films. All NT arrays prepared with anodization times above 20 min show only the reflections characteristic of the anatase crystal structure. In contrast, the sample prepared by a 10 min anodization (i.e., the thinner sample of the series) exhibits the reflections of rutile as well, due to the fact that rutile grows at the interface between metallic Ti and the NT bottom, where the metal undergoes thermal oxidation during the calcination process.[6,8] The series of NT arrays obtained at different applied potentials (30–80 V) by adjusting the anodization time so as to keep the NT length fixed at 1 μm shows similar XRD patterns (Figure S3 in the Supporting Information), typical of pure anatase. Thus, the

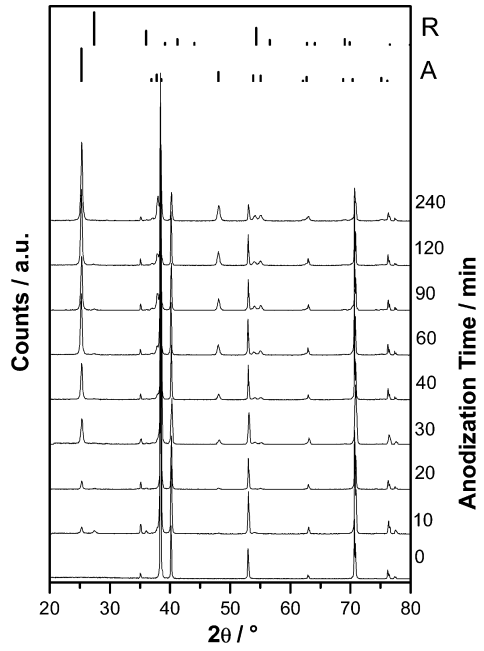

Figure 5. XRD patterns of pristine Ti foil and of TiO_2 NT films grown by anodization at 50 V for different times, followed by calcination at 450 °C. The peak positions and relative intensities of anatase (A) and rutile (R) are reported at the top of the figure for comparison. The first pattern at the bottom (0 min anodization time) corresponds to that of the metal Ti foil.

applied voltage does not affect the crystallinity of the film because it does not affect the TiO_2 NT wall thickness and because the crystallinity is due to the postthermal treatment.

3.3. Diffuse Reflectance UV–Vis–NIR Spectroscopy. The UV–vis–NIR DR spectra recorded in the 220 nm < λ < 2600 nm range are shown in Figure 6, as functions of the

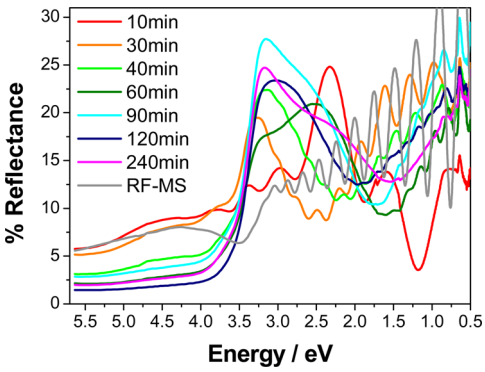

Figure 6. UV–vis–NIR DRS spectra of TiO_2 NT films grown by anodization at 50 V for different times, followed by calcination at 450 °C. The spectrum of an anatase TiO_2 dense film prepared by RF-magnetron sputtering (gray curve) is also shown for comparison.

photon energy. In the vis–NIR region the NT thin films synthesized with anodization times up to 60 min display the typical fringes originated by the interference of waves reflecting off the top surface with those propagating through the film and reflecting from the bottom surface. The frequency of the fringes increases and their amplitude decreases with increasing film thickness. The interference fringes originate only in thin films and they vanish in thick films, depending on the photon penetration depth. Hence, no interference fringes can be

DOI: 10.1021/acscatal.5b02817
ACS Catal. 2016, 6, 1345–1353

observed in the spectra of powder materials. For TiO_2 films the fringes usually vanish above 2 μm, as in the case of the samples prepared at 120 and 240 min.

From the interference fringes it is possible to calculate the film thickness d (i.e., the NT length) as follows. The reflectance is approximately π periodic in kd (where k is the component of the wavevector normal to the film); i.e., if λ_1 and λ_2 are two consecutive peaks or valleys wavelengths, the following equation holds:

$$2\left(\frac{1}{\lambda_1} - \frac{1}{\lambda_2}\right) n(\cos\phi')d = 1$$

where n is the refractive index of the film (ca. 2.5 for anatase in the range 450−600 nm) and ϕ' the angle of refraction. Using Snell's law to replace ϕ' with the incidence angle, ϕ, one obtains

$$d = \frac{1}{2\sqrt{n^2 - n_a^2 \sin^2\phi}} \frac{\lambda_1\lambda_2}{\lambda_1 - \lambda_2}$$

where n_a is the refractive index of the incidence medium (n_a = 1 for air). This result holds irrespective of the properties of the supporting substrate (e.g., Ti), provided its reflectivity is approximately constant in the spectral region of interest. The d values calculated by this equation are in very good agreement with the NT length determined by SEM analysis (see Figure 2).

Also reported in Figure 6 is the DR spectrum of a ca. 1 μm thick film consisting of randomly packed TiO_2 anatase nanoparticles produced by radio frequency magnetron sputtering (gray curve in Figure 6). The NT films display increased reflectance just before the semiconductor absorption threshold that might be due to the overlapping with the photonic band gap. Such an increase in reflectance does not occur in the dense film made by magnetron sputtering, because it does not have photonic crystal properties.

The absorption edge of the NT films are all located around 3.2 eV, which is typical of bulk anatase, independently of the anodization time or applied voltage (see also Figure S4 in the Supporting Information). Overlapping of the absorption edge with the interference fringes is particularly evident in the case of the thinner film (10 min anodization time). Moreover, the absorption step increases and the reflectance in the UV region decreases with an increase in the anodization time (i.e., the film thickness) up to 2 μm thick films (obtained by 90 min anodization time). This suggests that ca. 2 μm is the maximum penetration depth of the incident light in TiO_2 NTs.

3.4. Photonic Band Gap Theoretical Calculations. The typical photonic band structure calculated for a 35 nm NT inner radius is shown in Figure 7. Only the first few modes are shown as a function of the photon momentum. The resulting dispersion for the lowest mode (the light mode) is linear for small momenta, and it shows a forbidden band gap where light cannot propagate through the structure. This photonic gap adds to the optical gap (the frequency region where photon propagation is prevented by optical absorption) and may modify the absorption properties of the dielectrics, especially at the threshold.

In the case of Figure 7 the interval of forbidden photon energies is located at about 4.5 eV: i.e., above the TiO_2 anatase absorption threshold (ca. 3.2 eV). The obtained value is likely overestimated, because a frequency-independent dielectric permittivity was used for anatase. In fact, the solver

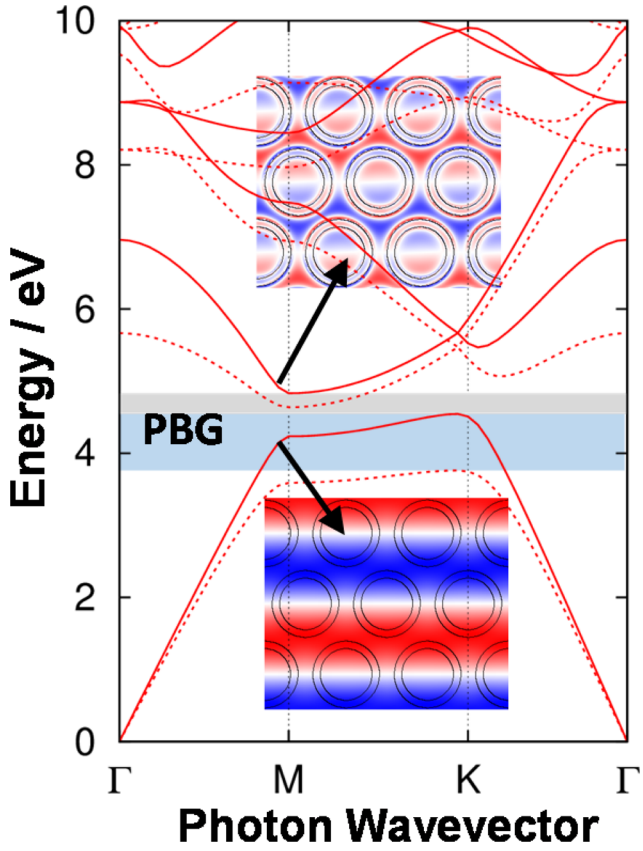

Figure 7. Photonic bands structure of TiO_2 NT arrays with 35 nm inner radius, 10 nm wall thickness, and 20 nm gap between the tubes calculated with ε = 7.1 (solid lines) or ε = 11.7 (dotted lines). The photonic band gap is highlighted by gray and light blue stripes. The two insets show the electromagnetic field localization at the air and dielectric bands.

implemented in the MIT photonic bands code (MPB)[24] does not allow either the frequency dependence or an imaginary part of the dielectric permittivity. For example, Figure 7 shows that when the dielectric permittivity of anatase at 4 eV is used during the calculation (ε = 11.7) the PBG widens and shifts toward lower energy. Despite these limitations (light traveling parallel to the film, nondispersive and nonabsorbing TiO_2), very important qualitative information can be obtained on the dependence of the photonic band gap position on geometrical parameters (Figure 8). Indeed, the simulations show that the photonic gap shifts to lower energy (higher wavelength) as the tube radius increases (Figure 8A).

For a tube inner radius larger than 50 nm the computed photonic gap falls below the anatase absorption threshold. Interestingly, there is a maximum value for the tube radius, beyond which the photonic gap vanishes. The band gap also shifts to lower energy and widens as the tube thickness increases (Figure 8B). In this case, there is a minimum thickness, below which the photonic gap closes. The dependence of the photonic gap is less affected by the spacing of the tubes (Figure 8C), but if the tubes are made further apart, the calculation predicts a vanishing band gap. Therefore, there is a very good agreement on a quantitative level between the present experimental results and calculations, and a photonic band gap is expected for hollow tubes in a narrow range of geometric parameters (radius, thickness, and distance), around those reported in this work. Moreover, the most important

DOI: 10.1021/acscatal.5b02817
ACS Catal. 2016, 6, 1345−1353

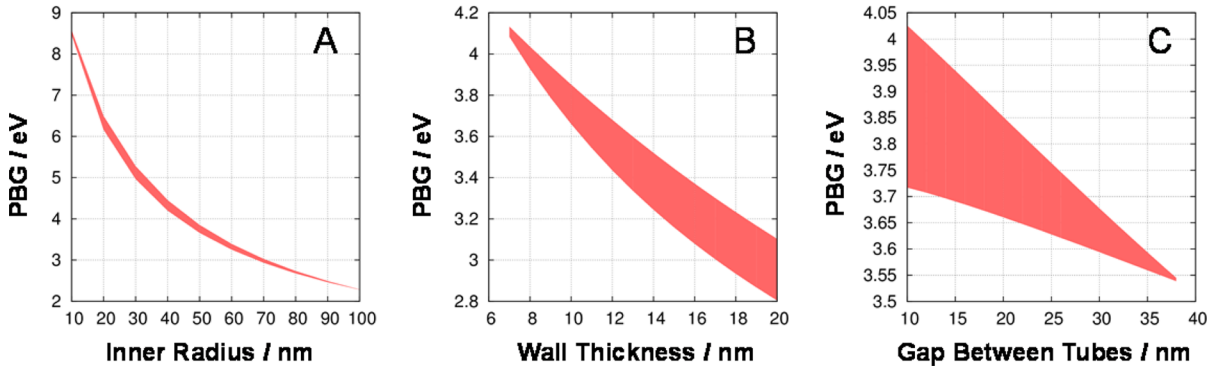

Figure 8. Effect on the PBG position of TiO_2 NT (A) inner radius, (B) tube thickness, and (C) gap between tubes.

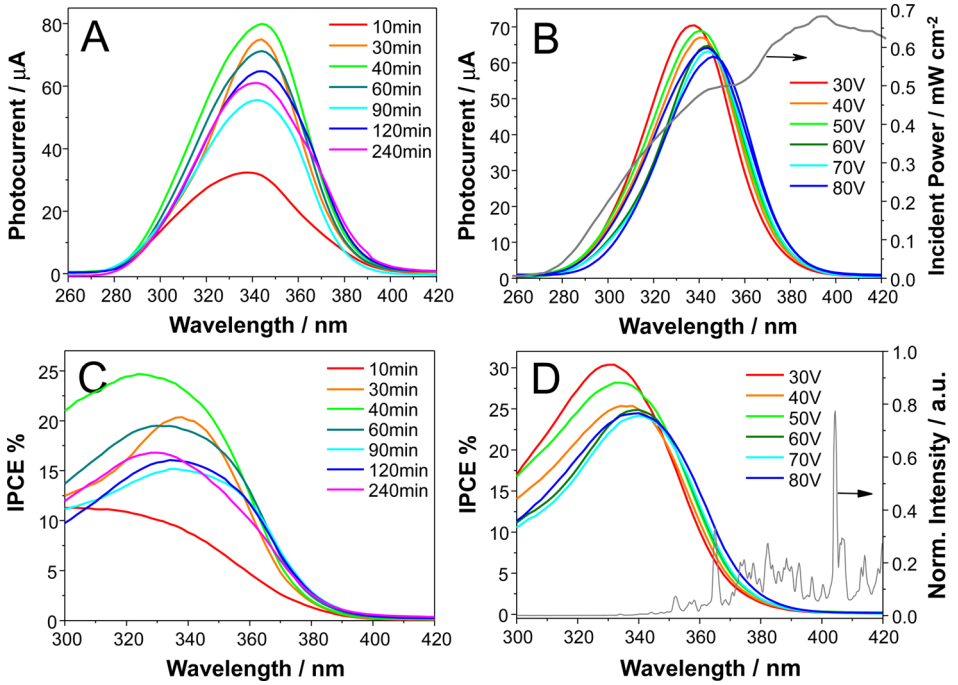

Figure 9. Effect of (A, C) anodization time and (B, D) applied potential on (A, B) photocurrent and (C, D) IPCE as a function of the incident wavelength. The gray curves in B and D are the incident power of the Xe lamp used for the IPCE measurements and the spectrum of the Hg vapor lamp used for separate H_2 and O_2 evolution photocatalytic tests, respectively.

result arising from these calculations is the possibility of tuning and engineering the PBG position so that it falls in the most convenient photonic energy position, by simply adjusting the proper TiO_2 NT synthesis parameters.

Figure 7 also shows the localization of the electromagnetic field at the blue (air band) and red (dielectric band) edges of the PBG. As already mentioned above, at the high-energy band the light traveling perpendicular to the NT arrays is predominantly localized in the empty spaces: i.e., air or water (low dielectric medium). In contrast, at the low-energy band the light is predominantly focused on the TiO_2 NT walls (high dielectric medium), leading to an increased photonic density on the semiconductor material. This is a peculiar characteristic of photonic crystals. Indeed, in dense and randomly packed films of TiO_2 nanoparticles light propagates as a flat wave.

3.5. IPCE Measurements. The photocurrent curves measured as a function of the incident wavelength exhibit a Gaussian-like shape (Figure 9A,B). The photocurrent increases with increasing wavelength because of the increasing incident light power (gray curve in Figure 9B) followed by a photocurrent decrease above the semiconductor absorption edge. All films prepared by increasing the anodization time show a photocurrent maximum located at 344 nm.

As shown in Figure 9C and in Figure S5 in the Supporting Information, at the beginning the maximum IPCE linearly increases with an increase in the anodization time (i.e., with an increase in the NT length), reaching a maximum of 25% for the NT array anodized for 40 min (1 μm length). Above this time the maximum IPCE slightly decreases and reaches a plateau above 90 min (2 μm length). The initial maximum IPCE growth can be ascribed to the increasing NT length, leading to a surface area and incident photon absorption efficiency enhancement up to the maximum light penetration depth (i.e., 2 μm, as suggested by the DR analysis in Figure 6).

Above this limit the maximum IPCE decreases because the beneficial effect of further surface area growth is compensated by the longer percolation path for photopromoted electron transfer, with a consequent higher probability of electron−hole recombination. Moreover, longer NTs can introduce mass transfer limitations due to penetration and diffusion of the

DOI: 10.1021/acscatal.5b02817
ACS Catal. 2016, 6, 1345−1353

Table 1. Effect of Applied Potential during the Anodization Synthesis of the TiO_2 NTs Array Films on the H_2 (r_{H_2}) and O_2 (r_{O_2}) Production Rates and on the Expected Quantum Efficiency (ϕ_{exp})

		r_{H_2}/mmol h^{-1}			
applied potential/V	anodization time/min	from evolved gas	from photocurrent	ϕ_{exp}/%	r_{O_2}/mmol h^{-1}
30	72	0.101	0.110	4.43	0.023
40	54	0.120	0.122	4.70	0.039
50	43	0.133	0.142	5.30	0.029
60	36	0.140	0.147	5.38	0.033
70	31	0.132	0.144	5.39	0.033
80	27	0.153	0.154	5.95	0.042

electrolyte and of the produced O_2 along the NT pores.[29] These results demonstrate that the optimal NT length under the investigated preparation conditions is 1 μm. On the basis of this result, the second series of films was prepared at different applied potentials by adjusting the anodization time in order to keep the NT length fixed at ca. 1 μm (Table 1). This allowed a systematic investigation of the effect of the sole tube diameter on the photocatalytic performance of the NT arrays. The so obtained photocurrent measurements and IPCE results are presented in Figure 9B,D, respectively. All photocurrent curves are characterized by a similar magnitude in agreement with the similar NT length (Figure 9B). The maximum of the IPCE at first decreases from 30% and then stabilizes to ca. 25% with an increase in the NT pore diameters (Figure S6 in the Supporting Information). This trend can be explained by considering that an increase in the pore diameters on one hand decreases the specific surface area (i.e., the surface active sites) but on the other hand diffusion, mass transfer, and photon penetration along the NT pores improve. However, the most relevant result is the red shift of the photocurrent curves (Figure 9B) with increasing NT pore diameter that likewise provokes a red shift of the photoactivity threshold (Figure 9D), as underlined by the linear variation of the first-derivative minimum of the IPCE curves (Figure S6). This result, achieved by simply changing the pore diameter without any chemical doping or electronic structure variation, has an important effect on the frame of solar light harvesting and conversion. In particular, the red shift can be explained by considering the parallel red shift of the PBG position: i.e., the IPCE threshold moves with the dielectric band maximum, where an increased photon absorption efficiency is expected because of the generation of slow photons and the localization of the electromagnetic field on the TiO_2 NT walls. In contrast, at the high-energy band (at shorter wavelengths) the electromagnetic field is predominantly localized in water, causing a photocurrent decrease with an increase in the TiO_2 NT pore diameter. Because these films have similar thicknesses and compositions and are illuminated perpendicularly (i.e., coaxially with respect to the NTs), we can expect a similar optical response with respect to the directly incident photons. Thus, the remarkable differences observed in the IPCE threshold position can be explained in terms of photonic crystal properties only considering that *diffuse light* (i.e., light traveling more or less orthogonal to the NTs) plays a crucial role in determining the photocatalytic performance of our NT arrays in the TiO_2 absorption edge region. Light scattering might occur because of local defects in the real NT array framework and arrangement, and it is also favored by the intrinsic divergence (ca. 4°) of the adopted light source. In other words, the photoactivity response is strongly determined by the many scattering processes that can occur within the illuminated area of the sample.

Notice that the argument can be qualitative only, since the exact position of the PBG varies with the angle and the frequency of the incident photons (it shifts toward the blue when the frequency is decreased and the out-of-plane component of the photon momentum is increased).

3.6. Effect of the Angle of Incident Light. The effect of the incident angle on the photocurrent as a function of the photon wavelength is presented in Figure 10. The incident angle remarkably affects the photocurrent profile of the film prepared at 80 V. An almost linear increase of the photocurrent maximum at 350 nm can be observed with an increase in the incident angle up to 45° (from 63.7 μA at 0° up to 74.0 μA at 45°) followed by a slight decrease (70.8 μA) at 60°. In contrast, a minor effect of the incident angle was observed on the film prepared at 30 V. In this case the photocurrent maximum decreases from 77.8 μA at 0° to 76.1 μA at 15° and then rises again up to 79.1 μA at 60°.

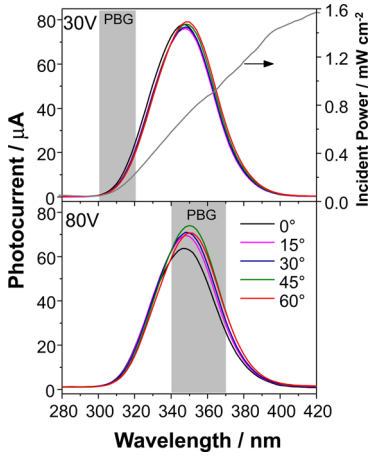

Figure 10. Effect of incident light angle on the photocurrent profile measured on the TiO_2 NT films prepared by anodization at 30 and 80 V applied potential. The gray curve in the upper panel is the incident light power.

The two films have similar thicknesses and differ only in the inner tube diameter and consequently in the PBG position. The film prepared at 80 V possesses the largest NT diameter and the PBG is located at longer wavelengths, very likely around the absorption threshold. Thus, the PBG is able to affect the photocurrent production. In contrast, the sample prepared at 30 V has a PBG shifted to shorter wavelengths possibly close to the emission edge of our setup, as suggested by the theoretical calculations. Hence, the photonic crystal properties can only

DOI: 10.1021/acscatal.5b02817
ACS Catal. 2016, 6, 1345−1353

marginally affect the photocurrent response of this sample. Moreover, the increasing photocurrent maximum can be ascribed to the expected larger fraction of photons scattered toward the direction orthogonal to the NTs with an increase in the incident angle. This finding demonstrates the crucial role played by the scattered photons in improving the photocatalytic performance in a 2D ordered photonic crystal structure. Indeed, the larger the fraction of photons scattered orthogonal to the NTs, the more the slow photons are able to enhance the photocurrent. Hence, the photocurrent of the sample prepared at 80 V increases with the incident angle and shifts toward the red, a remarkable behavior which is absent for the sample prepared at 30 V in the investigated spectral region.

Finally, the slight photocurrent decrease at 60° of the film prepared at 80 V can be attributed to the significant increase of specular reflection (Figure 11 and Figure S8 in the Supporting Information) recorded around the absorption edge (possibly related to the presence of the PBG in this region) with respect to the sample prepared at 30 V, causing a partial loss of incident photons.

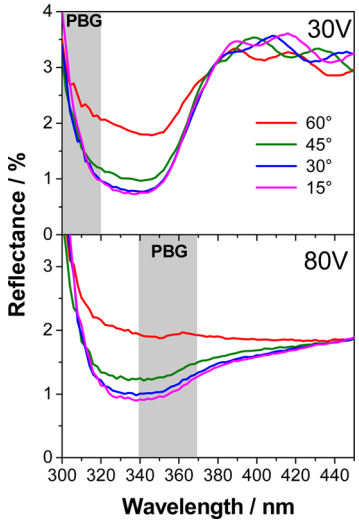

Figure 11. Specular percent reflectance spectra as a function of incident angle of TiO_2 NT films prepared at 30 and 80 V anodization voltage.

3.7. Separate H_2 and O_2 Production. In the previous section we showed that an increase in the NT inner diameter leads to a red shift of the IPCE curves (Figure 9D) thanks to the parallel shift of the PBG. These curves together with the emission spectrum of the employed light source (Figure 9D) can be used to calculate the *expected quantum efficiency in H_2 production* (ϕ_{exp}) under polychromatic irradiation (i.e., the "expected portion of converted spectrum"), obtained as the product of the IPCE curve times the emission spectrum of the lamp (Figure S9 in the Supporting Information). Thus, ϕ_{exp} can be calculated as the ratio of the integral of these curves over the integral of the whole incident spectrum in the $300 < \lambda < 400$ nm range. The obtained results are presented in Figure 12 and in Table1.

The H_2 production rates calculated by the produced gas collected in the graduated burets placed above the two electrodes are in agreement with those calculated by the photocurrent profiles (Figure S10 in the Supporting Information), as shown in Table1. Notice that H_2 evolves at a constant rate already after the first 1 h of irradiation, whereas

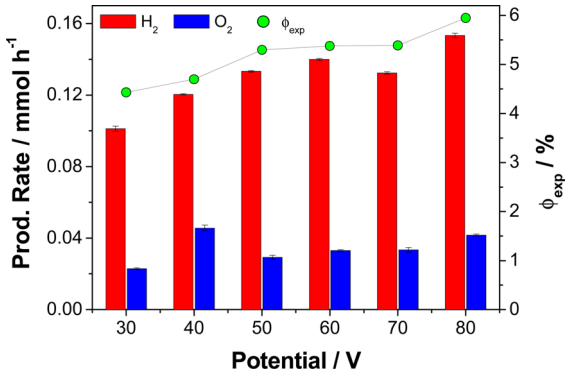

Figure 12. Effect of anodization applied potential on the rates of photocatalytic H_2 and O_2 production and on the expected quantum efficiency ϕ_{exp}.

O_2 evolution steadily increases during the first 3 h. As a consequence, the H_2:O_2 molar ratio approaches the expected stoichiometric value after this time (Figure S11 in the Supporting Information). This delayed O_2 evolution is likely due to its higher solubility in water with respect to hydrogen. Nevertheless, we cannot exclude that water is oxidized to O_2 through the intermediate formation of hydrogen peroxide, which is rather unstable in NaOH solutions and decomposes to O_2.

The H_2 production rate significantly increases with an increase in the NT inner diameter. In particular, a remarkable 50% increment of the H_2 production rate was attained by simply increasing the inner diameter from 35 nm (0.101 mmol of H_2 h^{-1}) to 70 nm (0.153 mmol of H_2 h^{-1}). Because the H_2 production rate follows the same trend as ϕ_{exp}, the improved photoactivity can be ascribed to the red shift of the IPCE curve that allows harvesting and converting a larger portion of the incident lamp spectrum thanks to the exploitation of the photonic crystal properties of the NT array film.

A similar effect of the anodization voltage on the H_2 production rate was recently reported by Sun and Yan,[10] who synthesized a series of NT films with the same anodization time at each applied potential and attributed the observed trend to the increased surface area consequent to the longer tubes. In contrast, here we are able to discern the effect of the sole inner diameter variation by comparing films with the same NTs length. This allows us to discuss our results in terms of photonic crystal properties, as supported by the IPCE measurements.

4. CONCLUSIONS

This work demonstrates that the photonic crystal properties typical of ordered periodic structures can be profitably exploited to increase the efficiency of solar light harvesting and conversion and the photocatalytic performance of TiO_2 NT arrays-based photoanodes. This can be attained by taking advantage of three characteristics of the photonic band structure: (i) the PBG can be used to confine the incident light of proper wavelength within the TiO_2 NTs film, (ii) the dielectric band can be used to concentrate the incident photons of corresponding wavelength on the TiO_2 NTs walls, and (iii) the absorption efficiency of these photons is further boosted by their reduced group velocity (slow photons) due to the flattening of the photonic band in certain propagation directions. Further performance improvement can be attained by tilting the incident light angle, hence increasing the fraction

DOI: 10.1021/acscatal.5b02817
ACS Catal. 2016, 6, 1345−1353

of photons scattered parallel to the film that can sense the photonic crystal properties. Theoretical calculations demonstrate that the position and width of the PBG are both affected by TiO_2 NT inner diameter, wall thickness, and distance between the pores. Thus, the PBG can be easily tuned by adjusting the TiO_2 NT synthesis parameters in order to fit with the semiconductor absorption band, aiming at red-shifting the photoactivity threshold. In this way a 50% higher H_2 production rate under polychromatic irradiation was attained by simply increasing the inner TiO_2 NT diameter. This important result can in principle be transferred to any other semiconductor material and can be exploited in the field of solar fuels production to harvest and convert a larger portion of the solar spectrum.

■ ASSOCIATED CONTENT

Supporting Information

The Supporting Information is available free of charge on the ACS Publications website at DOI: 10.1021/acscatal.5b02817.

Schematic representation of the setup used for studying the effect of incident light angle, XRD and UV−vis−NIR DRS of the series of TiO_2 NTs films prepared at different applied potential, and the expected portion of converted incident lamp spectrum and photocurrents measured during separate H_2 and O_2 photocatalytic tests (PDF)

■ AUTHOR INFORMATION

Corresponding Author

*E-mail for G.L.C.: gianluca.chiarello@unimi.it.

Notes

The authors declare no competing financial interest.

■ ACKNOWLEDGMENTS

The authors thank Dr. Daniele Mendola for his skillful collaboration in the preparation of TiO_2 NT arrays and Dr. Benedetta Sacchi for SEM analysis. Financial support from Regione Lombardia and Cariplo Foundation (Grant No. 2013-1766) within the SmartMatLab Centre project is gratefully acknowledged.

■ REFERENCES

(1) Lu, Y.; Yu, H.; Chen, S.; Quan, X.; Zhao, H. *Environ. Sci. Technol.* **2012**, *46*, 1724−1730.
(2) Li, J.; Wu, N. *Catal. Sci. Technol.* **2015**, *5*, 1360−1384.
(3) Lianos, P. *J. Hazard. Mater.* **2011**, *185*, 575−590.
(4) Walter, M. G.; Warren, E. L.; McKone, J. R.; Boettcher, S. W.; Mi, Q.; Santori, E. a.; Lewis, N. S. *Chem. Rev.* **2010**, *110*, 6446−6473.
(5) Selli, E.; Chiarello, G. L.; Quartarone, E.; Mustarelli, P.; Rossetti, I.; Forni, L. *Chem. Commun.* **2007**, 5022−5024.
(6) Altomare, M.; Pozzi, M.; Allieta, M.; Bettini, L. G.; Selli, E. *Appl. Catal., B* **2013**, *136−137*, 81−88.
(7) Roy, P.; Berger, S.; Schmuki, P. *Angew. Chem., Int. Ed.* **2011**, *50*, 2904−2939.
(8) Mor, G. K.; Varghese, O. K.; Paulose, M.; Shankar, K.; Grimes, C. a. *Sol. Energy Mater. Sol. Cells* **2006**, *90*, 2011−2075.
(9) Xue, Y.; Sun, Y.; Wang, G.; Yan, K.; Zhao, J. *Electrochim. Acta* **2015**, *155*, 312−320.
(10) Sun, Y.; Yan, K. P. *Int. J. Hydrogen Energy* **2014**, *39*, 11368−11375.
(11) Regonini, D.; Clemens, F. J. *Mater. Lett.* **2015**, *142*, 97−101.
(12) Lynch, R. P.; Ghicov, A.; Schmuki, P. *J. Electrochem. Soc.* **2010**, *157*, G76−G84.
(13) Joannopoulos, J. D.; Villeneuve, P. R.; Fan, S. *Nature* **1997**, *386*, 143−149.
(14) Chen, J. I. L.; von Freymann, G.; Choi, S. Y.; Kitaev, V.; Ozin, G. A. *J. Mater. Chem.* **2008**, *18*, 369−373.
(15) Chen, J. I. L.; Von Freymann, G.; Choi, S. Y.; Kitaev, V.; Ozin, G. A. *Adv. Mater.* **2006**, *18*, 1915−1919.
(16) Chen, H.; Chen, S.; Quan, X.; Zhang, Y. *Environ. Sci. Technol.* **2010**, *44*, 451−455.
(17) Wu, M.; Liu, J.; Jin, J.; Wang, C.; Huang, S.; Deng, Z.; Li, Y.; Su, B. L. *Appl. Catal., B* **2014**, *150−151*, 411−420.
(18) Liu, J.; Liu, G.; Li, M.; Shen, W.; Liu, Z.; Wang, J.; Zhao, J.; Jiang, L.; Song, Y. *Energy Environ. Sci.* **2010**, *3*, 1503.
(19) Chen, J. I. L.; Ozin, G. a. *J. Mater. Chem.* **2009**, *19*, 2675.
(20) Sordello, F.; Minero, C. *Appl. Catal., B* **2015**, *163*, 452−458.
(21) Sordello, F.; Duca, C.; Maurino, V.; Minero, C. *Chem. Commun.* **2011**, *47*, 6147−6149.
(22) Zhang, Z.; Zhang, L.; Hedhili, M. N.; Zhang, H.; Wang, P. *Nano Lett.* **2013**, *13*, 14−20.
(23) Al-Haddad, A.; Wang, Z.; Xu, R.; Qi, H.; Vellacheri, R.; Kaiser, U.; Lei, Y. *J. Phys. Chem. C* **2015**, *119*, 16331−16337.
(24) Johnson, S.; Joannopoulos, J. *Opt. Express* **2001**, *8*, 173−190.
(25) Jellison, G. E.; Boatner, L. a.; Budai, J. D.; Jeong, B. S.; Norton, D. P. *J. Appl. Phys.* **2003**, *93*, 9537−9541.
(26) Albu, S. P.; Ghicov, A.; Aldabergenova, S.; Drechsel, P.; LeClere, D.; Thompson, G. E.; Macak, J. M.; Schmuki, P. *Adv. Mater.* **2008**, *20*, 4135−4139.
(27) Macak, J. M.; Albu, S. P.; Schmuki, P. *Phys. Status Solidi RRL* **2007**, *1*, 181−183.
(28) Apolinário, A.; Quitério, P.; Sousa, C. T.; Ventura, J.; Sousa, J. B.; Andrade, L.; Mendes, a. M.; Araújo, J. P. *J. Phys. Chem. Lett.* **2015**, *6*, 845−851.
(29) Kim, D.; Macak, J. M.; Schimidt-Stein, F.; Schmuki, P. *Nanotechnology* **2008**, *19*, 305710.

DOI: 10.1021/acscatal.5b02817
ACS Catal. 2016, 6, 1345−1353